Article

Nanostructured Equimolar Ceria-Praseodymia for Total Oxidations in Low-O$_2$ Conditions

Enrico Sartoretti [1][ID]**, Fabio Martini [2,3], Marco Piumetti [1], Samir Bensaid [1,*], Nunzio Russo [1] and Debora Fino [1]**

[1] Department of Applied Science and Technology, Politecnico di Torino, Corso Duca degli Abruzzi 24, 10129 Turin, Italy; enrico.sartoretti@polito.it (E.S.); marco.piumetti@polito.it (M.P.); nunzio.russo@polito.it (N.R.); debora.fino@polito.it (D.F.)

[2] Department of Chemistry and Industrial Chemistry, Università di Pisa, Via G. Moruzzi 13, 56124 Pisa, Italy; fabio.martini@sns.it

[3] Scuola Normale Superiore, Piazza dei Cavalieri 7, 56126 Pisa, Italy

* Correspondence: samir.bensaid@polito.it; Tel.: +39-011-090-4662

check for updates

Abstract: A Gasoline Particulate Filter (GPF) can be an effective solution to abate the particulate matter produced in modern direct injection gasoline engines. The regeneration of this system is critical, since it occurs in oxygen deficiency, but it can be promoted by placing an appropriate catalyst on the filter walls. In this paper, a nanostructured equimolar ceria-praseodymia catalyst, obtained via hydrothermal synthesis, was characterized with complementary techniques (XRD, N$_2$-physisorption, FESEM, XPS, Temperature Programmed Reduction, etc.) and its catalytic performances were investigated in low oxygen availability. Pr-doping significantly affected ceria structure and morphology, and the weakening of the cerium–oxygen bond associated to Pr insertion resulted in a high reducibility. The catalytic activity was explored considering different reactions, namely CO oxidation, ethylene and propylene total oxidation, and soot combustion. Thanks to its capability of releasing active oxygen species, ceria-praseodymia exhibited a remarkable activity and CO$_2$-selectivity at low oxygen concentrations, proving to be a promising catalyst for coated GPFs.

Keywords: doped ceria; ceria-praseodymia catalyst; nanostructures; CO oxidation; soot oxidation; VOCs oxidation; low oxygen availability; GPF

1. Introduction

In the recent years, several strategies have been implemented by automotive manufacturers in order to comply with the CO$_2$ emission targets imposed by many nations (e.g., 95 g/km in the European Union by 2021) [1]. Diesel engines provide a good efficiency, but they require a complex after-treatment apparatus [2] and they have encountered a decline in popularity in recent years; hence, many efforts have been devoted to improving the overall fuel economy of gasoline engines. Among the different solutions developed, the Gasoline Direct Injection (GDI) technology presents several advantages with respect to Port Fuel Injection (PFI), since a GDI engine can work with higher efficiency and lower fuel consumption [3]. However, the reduced degree of mixing in the combustion chamber entails the production of a greater range and quantity of noxious combustion by-products in the fuel-rich regions of the flame, e.g., unburned hydrocarbons and carbonaceous particulate matter (soot) [3–6]. Since the actual regulations strictly limit not only the mass but also the number of solid particles that can be emitted, GDI vehicles have been equipped with a Gasoline Particulate Filter (GPF) in order to keep the emissions within the limits [1,5,7]. The structure and operating principle of a GPF are similar to that of a Diesel Particulate Filter (DPF), but the regeneration phase is more critical due to the lack of

oxygen. In fact, while the O_2 concentration is usually around 10% in Diesel exhaust, it is lower than 5% in stratified-charge GDI engines and it is barely measurable in homogeneous-charge GDI engines, due to the stoichiometric air-to-fuel ratio employed [8].

In order to lower the temperature and time required for the GPF regeneration, as well as the associated fuel consumption, a catalytic coating can be placed on the filter walls with the purpose of promoting soot oxidation. To this end, ceria-based catalysts have been widely investigated, thanks to the interesting physico-chemical properties and redox cycle typical of these materials [9–11]. In fact, cerium's ability to easily change its oxidation state from Ce^{4+} to Ce^{3+} is associated with a high Oxygen Storage Capacity (OSC), i.e., the possibility of releasing oxygen species, which can be exploited to oxidize different pollutants (e.g., CO or soot). Moreover, ceria nanoparticles with tailored shape can be obtained by tuning the synthesis conditions [12]. The morphology plays a key role in defining ceria activity, because it affects not only the specific surface area and exposed crystal planes, but also the type and quantity of solid–solid contact points in the case of the soot oxidation [12–15].

Ceria properties can be further tuned by inserting certain dopant ions into its crystal structure, in order to improve the activity and stability of the catalytic system. The addition of a foreign element promotes the formation of different kinds of defects in ceria lattice, e.g., oxygen vacancies, which have been recognized to play an active role during catalysis [16–20]. In fact, the oxidation reactions are believed to occur via a Mars–van Krevelen-type mechanism over ceria-based catalysts, involving the formation and refilling of oxygen vacancies [11,21]. Different transition metals and rare earth elements have been studied as dopants and promising results in terms of soot oxidation activity have been obtained with praseodymium [22,23]. In particular, nanostructured equimolar Ce–Pr mixed oxide was even able to outperform a supported Pt-based catalyst [24,25]. Although this material has been thoroughly investigated under different conditions, a complete study in low oxygen availability is required to evaluate its application in a GPF.

In this paper, a nanostructured equimolar ceria-praseodymia catalyst was prepared via hydrothermal synthesis and was characterized with several techniques in order to evaluate its textural, morphological and physico-chemical properties. The catalytic activity was explored considering different reactions, namely CO oxidation, ethylene and propylene total oxidation, and soot combustion. The tests were performed keeping an O_2 concentration of 1%, a value representative of a GDI engine exhaust [5], and the performances in oxygen, oxygen-deficient and oxygen-rich conditions were compared. Finally, a kinetic study of the soot oxidation reaction was carried out, estimating the oxygen reaction order.

2. Results and Discussion

2.1. Catalyst Characterization

The synthesized material was investigated using different complementary techniques, in order to unveil its physico-chemical and textural properties. Figure 1 displays the powder XRD diffractogram of the Ce50Pr50 catalyst, compared with that of pure ceria prepared using the same synthesis procedure. The mixed oxide exhibits the typical pattern of the fluorite crystalline structure of ceria, marked by the presence of the (111), (200), (220), (311) and (222) planes [12,13,25–27], as can be seen in Figure 1. This similarity indicates that Pr ions are well incorporated into the ceria lattice, which is confirmed by the absence of additional peaks, attributable to segregated oxides. However, the peaks in the XRD pattern of the Ce50Pr50 catalyst are slightly shifted towards lower angles with respect to those of pure ceria, and this displacement can be the result of lattice expansion. Actually, cerium and praseodymium cations have very similar ionic radii, but the latter element is more reducible; therefore, the observed shift is probably induced by the presence of Pr^{3+}, whose ionic radius is bigger than that of Ce^{4+} [28].
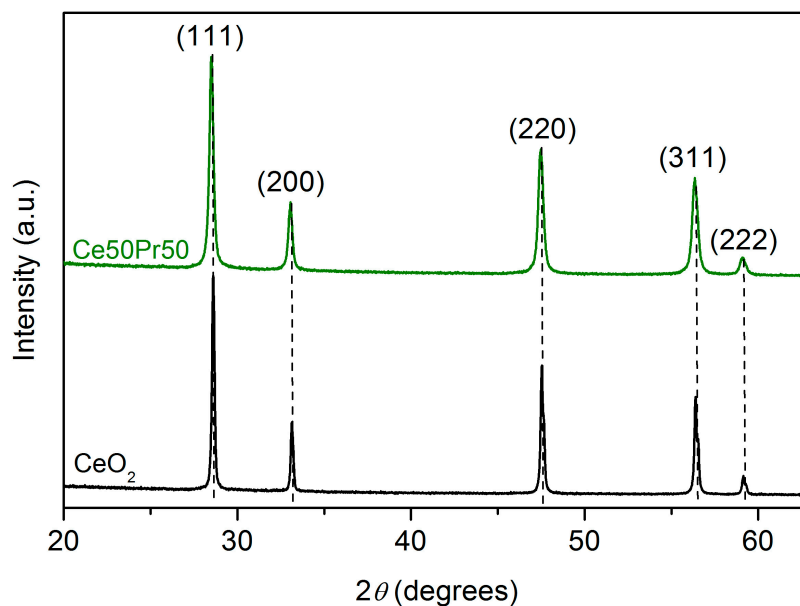
Figure 1. XRD diffractograms of the Ce50Pr50 catalyst and of pure ceria.

The (200)/(111) and (220)/(111) peak intensity ratios were calculated, and the values obtained were 0.32 and 0.63, respectively. Both these parameters are higher than those observed on pure ceria samples prepared in analogous conditions (being 0.30 and 0.51, respectively [12]), and especially the (220)/(111) ratio shows a remarkable increase. This result suggests that Pr addition can affect crystal growth during the synthesis, inducing an increase in the relative abundancy of the (110) planes. Furthermore, praseodymium addition was found to also influence the final dimension of the particles. Indeed, the average crystallite size was estimated using Scherrer's equation, and the value obtained for the Ce50Pr50 catalyst (42 nm) was significantly lower than that observed for pure ceria nanoparticles synthesized with the same procedure (139 nm).

The specific surface area of the Ce50Pr50 sample was calculated via nitrogen physisorption, using the BET method. A value of 13 m^2/g was found, slightly higher than that of pure CeO_2 (7 m^2/g), in agreement with the smaller size of the ceria-praseodymia crystallites pointed out by the XRD results.

Figure 2 reports some FESEM micrographs of the Ce50Pr50 catalyst, in which two different types of nanostructures can be noticed. Both nanopolyhedra and nanorods are present in the sample, instead of the nanocubes previously observed in pure ceria prepared using analogous synthesis conditions [12]. This confirms that Pr addition directly affects the ripening process, promoting the growth of (110) crystal planes and thus favoring edge truncation and elongation of the particles. Energy Dispersive X-ray analysis (EDX) was performed focusing the spot on different points of the sample. The average composition of the mixed oxide resulted to be very close to the nominal one, with 49.4% of cerium and 50.6% of praseodymium. Furthermore, EDX mapping, whose results are reported in Figure 3, showed that the two elements are evenly distributed in the space, confirming the good homogeneity of the Ce50Pr50 sample.

The oxygen species on the surface of the sample were investigated analysing the O 1*s* XP spectrum shown in Figure 4, in which two distinct peaks can be observed. The intense peak centered at 528.1 eV can be ascribed to lattice oxygen (the so-called "O_β") [29,30] and it is slightly shifted towards lower binding energy as a consequence of Pr addition [25]. The peak at higher binding energy (530.9 eV) is instead assigned to the various "O_α" capping oxygen species chemisorbed on the surface, e.g., hydroxyl (OH^-), carbonate (CO_3^{2-}), peroxide (O_2^{2-}) or superoxide (O^{2-}) ions [31,32]. The relative abundancy of the O_α species, calculated from the area of the deconvoluted peaks and reported in Table 1, proved to be significant. A high quantity of chemisorbed oxygen can foster oxygen mobility and spillover at the catalyst surface, with beneficial effects during the oxidation reactions [13]; in particular, reactive

oxygen species play a key role in the soot oxidation, in which a direct interaction between the two solid phases is limited by the few contact points.
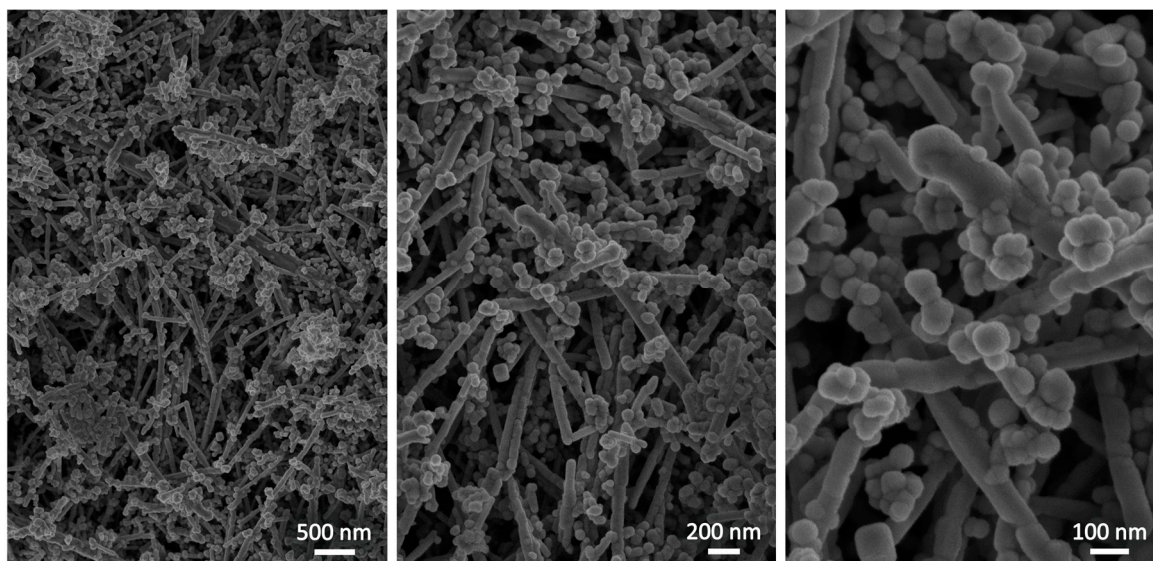

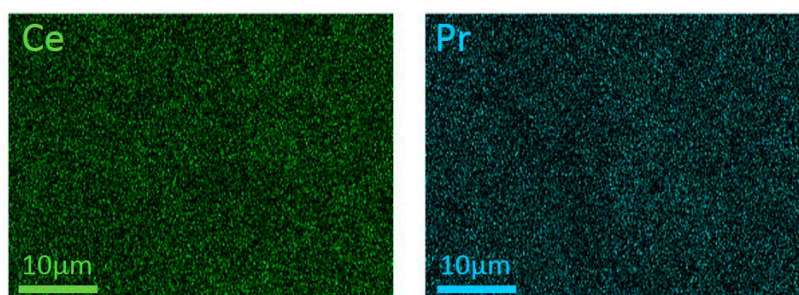**Figure 2.** FESEM images of the Ce50Pr50 catalyst.

Figure 3. EDX maps of the Ce50Pr50 catalyst showing the distribution of Ce and Pr ions.
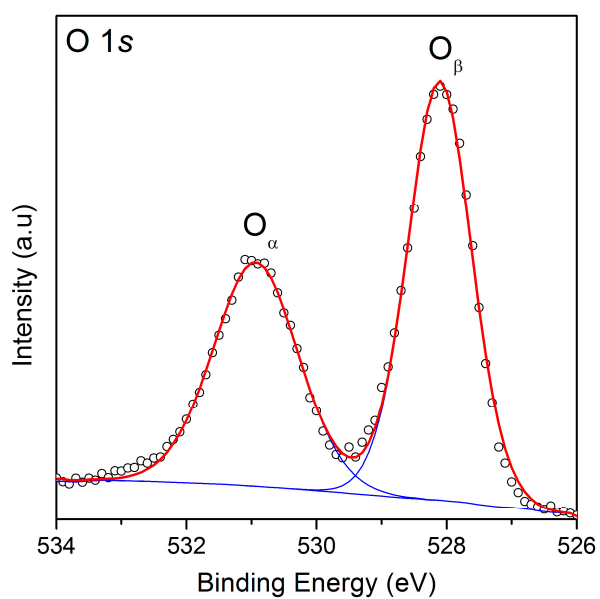

Figure 4. Deconvoluted XP spectrum of the Ce50Pr50 catalyst in the O 1s core level region.

Table 1. Relative abundancies of different species on the surface of the Ce50Pr50 catalyst derived from the deconvolution of the XP spectra.

O_α	O_β	Ce^{3+}	Ce^{4+}	Pr^{3+}	Pr^{4+}
41.6%	58.4%	19.3%	80.7%	63.8%	36.2%

Figure 5a depicts the Ce 3*d* core level region of the XP spectrum. Five "u" and five "v" peaks were identified, related to 3d$_{5/2}$ and 3d$_{3/2}$ states, respectively. The v°, v', u° and u' peaks were ascribed to Ce^{3+} ions, while the other six peaks were assigned to the 4+ oxidation state [33,34]. A similar deconvolution was performed on the Pr 3*d* XP spectrum, in the 968–923 eV region (Figure 5b), ascribing four peaks (herein denoted as a°, a', b° and b') to Pr^{3+} ions and other six peaks to the 4+ oxidation state [35]. The relative abundancy of the Ce and Pr cations was estimated after the deconvolution, and the calculated values are resumed in Table 1. Although Pr addition was proved to increase the Ce^{3+} quantity [25,36], cerium maintains 4+ as primary valence. Instead, most of the Pr cations are in the lower oxidation states, confirming the higher reducibility of this element and suggesting a strong presence of oxygen vacancies at the catalyst surface.
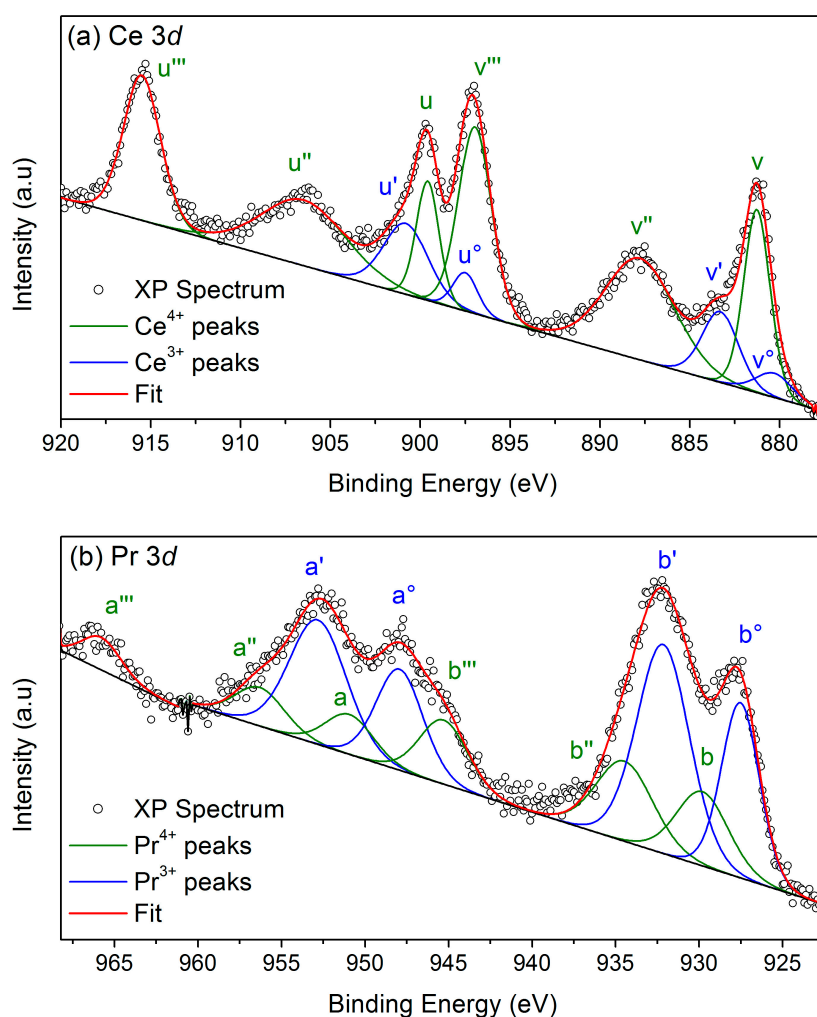

Figure 5. Deconvoluted XP spectra of the Ce50Pr50 catalyst in the (**a**) Ce 3d and (**b**) Pr 3d core levels regions.

In order to better investigate the reducibility of the catalyst, different types of Temperature Programmed Reduction (TPR) were performed. When H$_2$ is used, the TPR profile of pure ceria is

usually characterized by the presence of two peaks, since the reduction occurs in two steps. A lower temperature peak centered at 500–600 °C is associated to the surface reduction, while a band located above 700 °C is related to the slow release of bulk β-oxygen at very high temperatures [37,38]. For the Ce50Pr50 sample, a single intense peak was observed during the H_2-TPR, as reported in Figure 6a, pointing out that Ce and Pr ions are simultaneously reduced from a 4+ to a 3+ valence state. The position of this asymmetric component, centered around 460 °C, suggests that Pr addition significantly increases the ceria reducibility; in fact, the incorporation of Pr ions can weaken the Ce-O bond, thus fostering the oxygen release from both the surface and the bulk.
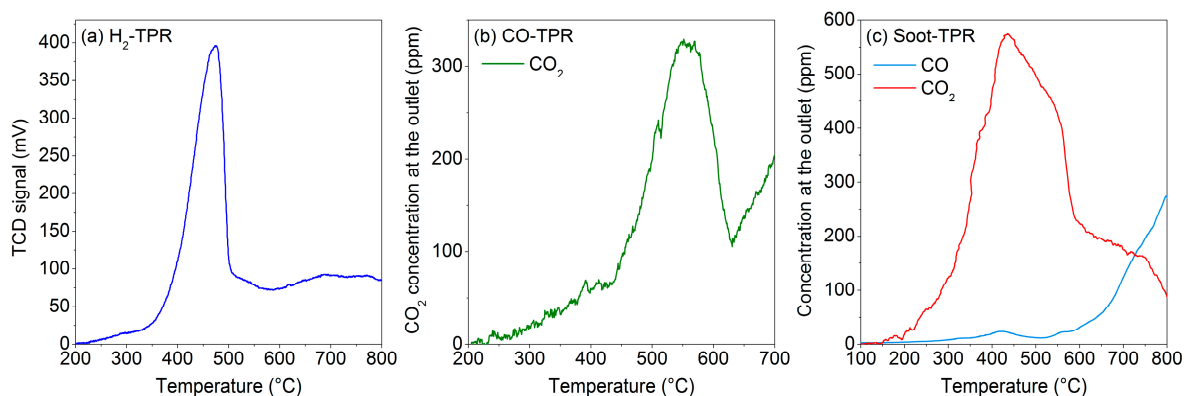

Figure 6. Results of the temperature programmed reduction analyses performed on the Ce50Pr50 catalyst: (**a**) H_2-TPR, (**b**) CO-TPR and (**c**) Soot-TPR.

The results of the CO-TPR are reported in Figure 6b. In this case, the CO_2 concentration at the outlet was monitored, as this species is the result of the reaction between the CO and the oxygen released from the catalyst lattice. While reduction peaks were barely visible for pure ceria nanocubes [36], here, a peak around 550 °C can be clearly observed for the Ce50Pr50 catalyst, as a result of its higher reducibility and OSC (the operating conditions adopted in this work differ from the ones of the CO-TPR reported in [23], and therefore the peak locates at a different temperature).

Furthermore, a soot–TPR analysis was performed, heating a bed of catalyst and soot in tight contact (i.e., mixed in a ball mill) in absence of gas-phase oxygen. The concentration profiles of the CO and CO_2 produced when the soot is oxidized by the catalyst are displayed in Figure 6c. Observing the plot, two reaction steps can be identified: at low temperatures (200–600 °C), when the surface oxygen species are still abundant, the catalyst reduction produces mainly CO_2 and almost no CO, pointing out the good selectivity of Ce50Pr50; however, at high temperatures (above 600 °C) more CO starts to be generated, since most of the available oxygen of the catalyst has already been consumed.

2.2. Catalytic Activity

The catalytic activity of nanostructured Ce50Pr50 was investigated by performing different oxidation reactions over the catalyst powder. The CO conversion, soot combustion and VOCs' total oxidation were tested in low oxygen concentration (1%), in order to simulate the conditions of a Gasoline Particulate Filter.

The oxidizing capability of the Ce50Pr50 catalyst was firstly evaluated through CO oxidation tests and compared to that of pure ceria. The results obtained, in terms of CO converted to CO_2 as a function of the temperature, are reported in Figure 7. In the absence of a catalyst, the thermal conversion of CO starts to be significant only above 500 °C, and it is still lower than 10% at 600 °C. However, this reaction can be activated at much lower temperatures by pure CeO_2, and the Ce50Pr50-mixed oxide shows even better catalytic performances. For a quantitative evaluation, the $T_{50\%}$ can be considered, namely the temperature at which 50% of the incoming CO is oxidized. The Ce50Pr50 sample was able to reach such a conversion at only 359 °C in high oxygen excess, exhibiting a specific reaction rate of

the CO oxidation of 47.16 $\mu mol_{CO}/h/m^2$ at this temperature, while the $T_{50\%}$ of pure CeO_2 was 413 °C. Nanostructured ceria-praseodymia is therefore more efficient towards CO abatement with respect to pure ceria [18,21,25] and to Pr-doped ceria synthesized with different techniques [27,39].
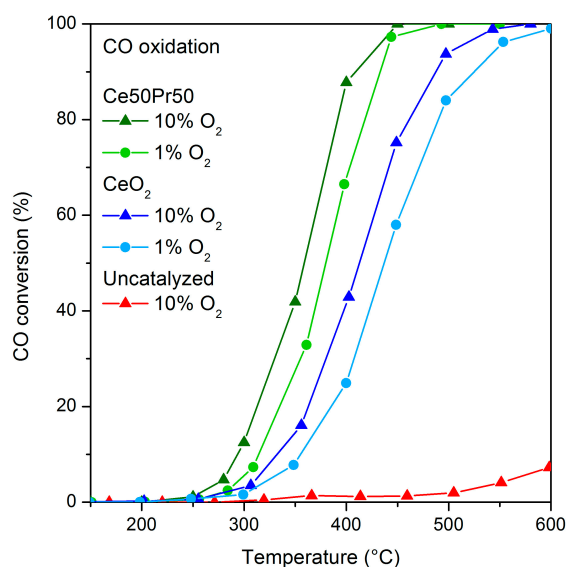

Figure 7. CO to CO_2 conversion as a function of the temperature, obtained testing pure CeO_2 and the Ce50Pr50 catalyst in different oxygen conditions.

The great activity of the Ce50Pr50 catalyst seems to be preserved even when the oxygen availability in the gas phase is limited: indeed, the conversion curve obtained in low-oxygen conditions is quite similar to that measured by feeding the reactor with 10% of oxygen, and the $T_{50\%}$ is just 20 °C higher (see Table 2). This interesting performance can be ascribed to the redox properties and high reducibility previously discussed. In fact, since CO oxidation occurs via a MvK-type mechanism over ceria-based catalysts [11], the ability to easily release surface oxygen species accessible to CO molecules plays a key role in defining the catalytic activity. Moreover, also the decrease in the particle size induced by Pr addition has a beneficial effect on the reaction, since the quantity of active sites available to the gaseous reagents is directly related to the specific surface area. Pure ceria also exhibited a limited shift in the CO conversion curve towards higher temperatures at low-oxygen conditions, presenting a $T_{50\%}$ of 437 °C.

Table 2. Comparison of the parameters obtained from the different catalytic tests performed in low-oxygen conditions (1% O_2) over the Ce50Pr50 catalyst and pure CeO_2. The temperatures at which 10%, 50% and 90% of conversion were reached ($T_{10\%}$, $T_{50\%}$ and $T_{90\%}$, respectively) are displayed.

Reaction	Catalyst	$T_{10\%}$ (°C)	$T_{50\%}$ (°C)	$T_{90\%}$ (°C)
CO oxidation	CeO_2	355	437	525
	Ce50Pr50	314	380	433
Ethylene oxidation	CeO_2	450	532	615
	Ce50Pr50	173	211	252
Propylene oxidation	CeO_2	370	475	543
	Ce50Pr50	255	327	389
Soot oxidation (tight contact)	CeO_2 [40]	431	485	527
	Ce50Pr50	408	465	582

In order to investigate the oxidizing activity of pure and Pr-doped ceria towards VOCs, ethylene and propylene were chosen as probe molecules. In fact, these two species are among the unburned hydrocarbons which can be found in the exhaust gas emitted by gasoline cars, since they can partially

slip away from the three-way catalyst at certain operative conditions [41]. The abatement of these compounds is of high importance due to the fact that some of them are toxic for human health [42–44] and they can also foster the photochemical generation of secondary pollutants, such as ozone [45]. Since ceria-based oxides can be used as catalysts [46–48] or noble metals supports [29,49,50] for VOCs' oxidation, CeO_2 and Ce50Pr50 are expected to affect these kinds of reactions.

The catalytic tests were carried out at two different concentrations of oxygen, in order to evaluate the effect of this parameter. The conversion curves resulting from the ethylene and propylene oxidation tests are reported in Figure 8. Both CeO_2 and Ce50Pr50 were able to catalyze the two oxidation reactions, since the temperatures required for the conversion were considerably lower in the presence of these catalysts with respect to the uncatalyzed tests. However, the mixed oxide showed a remarkably higher activity, as evidenced by the catalytic parameters resumed in Table 2.
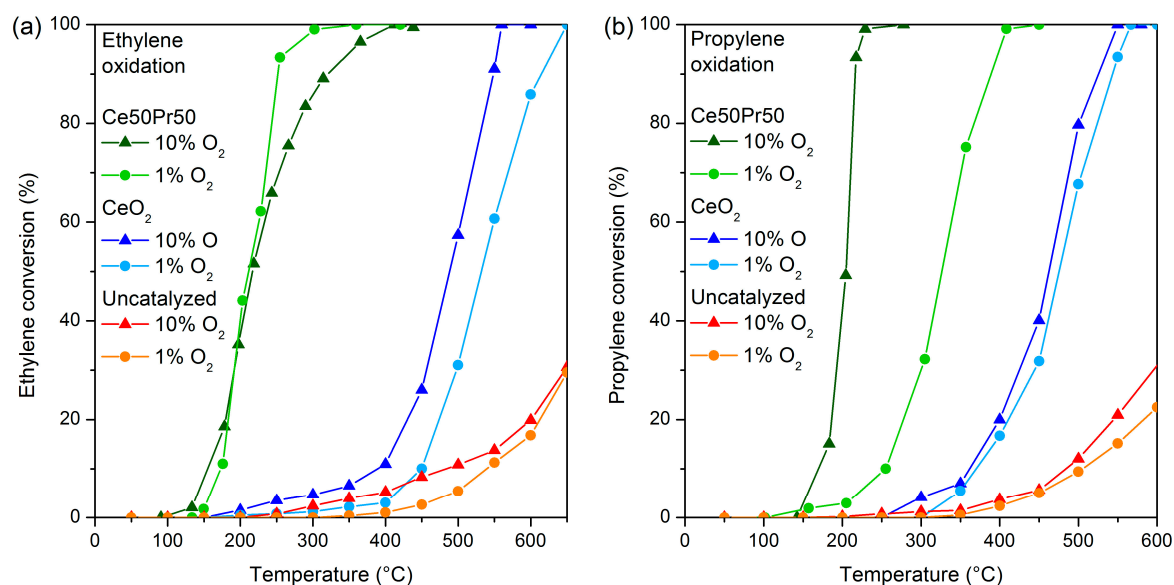

Figure 8. Ethylene (**a**) and propylene (**b**) conversion curves as a function of the temperature, obtained testing pure CeO_2 and the Ce50Pr50 catalyst in different oxygen conditions.

In the case of ethylene, pure ceria was more sensitive to the O_2 quantity, showing a lower conversion in oxygen shortage, as displayed in Figure 8a. Instead, the oxygen concentration induced only minimal changes on the conversion curve of Ce50Pr50: in fact, the light-off temperature was slightly lower when oxygen was in high excess, as could be expected, but then 50% of conversion was reached at about 215 °C regardless of the O_2 abundancy. At high temperatures, competitive adsorption between ethylene and oxygen might possibly explain the higher catalytic activity observed at a low oxygen concentration (1%): indeed, the higher conversion of ethylene could be due to its higher degree of adsorption on the catalyst with respect to the conditions at a high oxygen content (10%).

Conversely, oxygen availability seems to remarkably affect Ce50Pr50 performances in the case of propylene oxidation, as can be seen by observing Figure 8b. In detail, when 10% of oxygen was fed to the reactor, the Ce50Pr50 catalyst exhibited considerable activity, with a $T_{50\%}$ of 205 °C; under 1% of O_2, instead, 50% of conversion was reached at 327 °C, indicating that Ce50Pr50 is less active with a shortage of oxygen, although it is still able to significantly promote the propylene oxidation. On the contrary, the role of oxygen seems to be much less relevant for pure CeO_2, whose $T_{50\%}$ only slightly increased from 462 °C to 475 °C when reducing the oxygen concentration.

Furthermore, the Ce50Pr50 catalyst was also capable of affecting the selectivity to CO_2 during the VOCs' oxidation. The uncatalyzed reaction produces 25% of CO in the case of ethylene and 17% in the case of propylene oxidation (average values measured in the 300–500 °C range). When Ce50Pr50 is employed, instead, the CO formation is totally negligible in the case of ethylene (CO_2 selectivity is

always almost 100%), and it is marginal also when propylene is used, with a CO_2 selectivity ranging from 97% at 250 °C to values over 99% above 350 °C.

Afterwards, the activity of Ce50Pr50 towards the oxidation of particulate matter was evaluated. This heterogeneous reaction involves two solid phases, and is therefore strongly dependent on the quality of the contact at the interface, i.e., the force with which the two solids are brought together and the compatibility of their surface features [12,51–54]. For this reason, the catalytic activity was probed in two different conditions: loose contact (LC), which is more representative of the real situation in a GPF, was achieved by gently mixing the two powders with a spatula, while tight contact (TC), which can provide further information about the intrinsic activity, was reached via ball milling. Synthetic Printex-U carbon black was used as carbonaceous particulate, since it represents a suitable substitute for GDI soot [55], and 1% of O_2 was fed to the reactor.

The results of the soot oxidation tests are reported in Figure 9. As expected, better performances were observed at the higher degree of contact, but in both cases the catalyst was able to significantly reduce the temperature required for the soot conversion. Indeed, while 50% of the soot initially present was oxidized only at 652 °C without a catalyst, the same conversion was reached more than 100 °C earlier with Ce50Pr50: in detail, the $T_{50\%}$ was 510 °C in LC and 465 °C in TC. These values are comparable to those obtained at higher oxygen concentrations [25]. Instead, non-doped ceria exhibited a lower activity in oxygen shortage, since a higher $T_{50\%}$ of 485 °C was obtained when soot oxidation was performed in TC on this catalyst [40] (see Table 2).
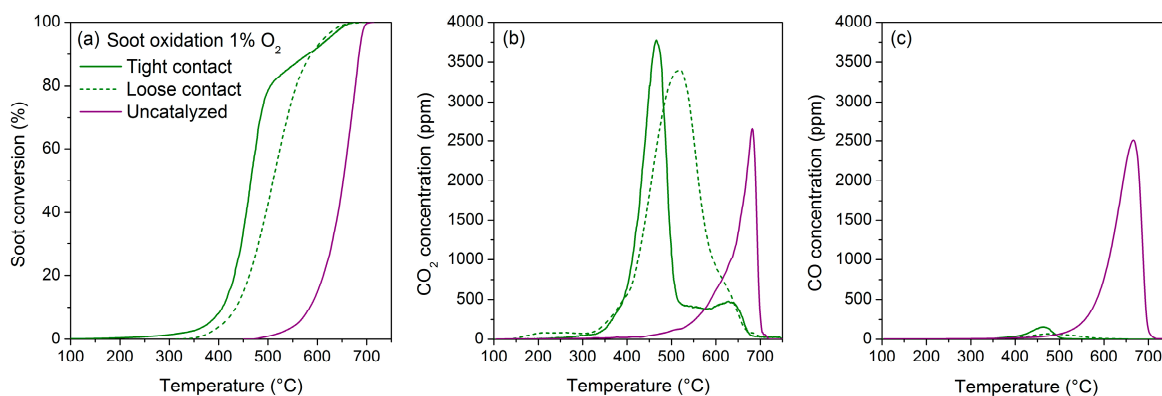

Figure 9. Soot conversion (**a**), CO_2 (**b**) and CO (**c**) concentration at the outlet as a function of the temperature during the soot oxidation tests performed over the Ce50Pr50 catalyst in low-O_2 conditions.

The Ce50Pr50 catalyst seems therefore able to interact effectively with the gas-phase O_2, even when the concentration of the latter is as low as 1%. As a result, this material was capable of preserving the selectivity towards CO_2 despite the low oxygen availability: indeed, when the soot combustion was performed in the absence of a catalyst, the carbon was converted mainly to CO, as the CO to CO_2 reaction step was hindered by the lack of gas-phase oxygen; instead, in the presence of Ce50Pr50, the CO_2 selectivity exceeded 96.5% in TC and reached 98% in LC.

Finally, kinetic studies were carried out in order to further analyze how the oxygen concentration affects the soot oxidation reaction when it is promoted by Ce50Pr50. The oxygen partial pressure in the gaseous mixture can be expected to affect the reaction rate, and will therefore feature in the rate equation with a certain reaction order. Kastrinaki et al. [56] described the isothermal oxidation of soot on ceria-based catalysts using a multi-population, first-order model: different oxidation rate constants were employed for different soot populations, which were distinguished by their contact conditions with the catalyst. Hence, the macroscopic oxidation process results from several parallel microscopic processes and can be modelled as follows

$$-\frac{dm}{dt} = \sum_n k_i \cdot m_i(t) \cdot [O_2]^\beta \tag{1}$$

with solutions of the type

$$m(t) = \sum_n m_{i,0} \cdot e^{-t/\tau_i} \tag{2}$$

with

$$\frac{1}{\tau_i} = k_i \cdot [O_2]^{\beta_i} \tag{3}$$

where m is the total soot mass, m_i is the soot mass of the i-th population, k_i is the rate constant for the oxidation in the contact conditions of the i-th population, β_i is the reaction order of oxygen for the i-th population and the subscript 0 indicates the initial soot mass. In tight contact, the contact conditions between the soot and the catalyst can be assumed to be homogeneous throughout the sample: the sum could therefore be reduced to a single term, and the macroscopic oxidation process can be effectively described by a monoexponential-type model

$$-\frac{dm}{dt} = k_{TC} \cdot m \cdot [O_2]^{\beta} \tag{4}$$

with a solution of the type

$$m(t) = m_0 \cdot e^{-t/\tau_{TC}} \tag{5}$$

The reaction order of oxygen can then be evaluated by carrying out isothermal oxidations at different oxygen partial pressures and by extracting the characteristic reaction times τ from monoexponential fittings of the soot conversion curves. In fact, extracting the logarithm from both members of equation (3) provides the following equation:

$$log(1/\tau_{TC}) = log(k_{TC}) + \beta log([O_2]) \tag{6}$$

The obtained τ values can be plotted against the respective values of the oxygen fraction in the gaseous mixture in a double logarithmic plot. A linear regression of the experimental points will provide a line whose slope is the reaction order of oxygen and whose intercept is the rate constant for tight contact conditions. This kind of kinetic evaluation was carried out by performing isothermal soot oxidation at 450 °C at three different O2 concentrations, namely 1%, 5% and 10%; the results of these tests are presented in Figure 10. The soot oxidation curves in Figure 10a point out the detrimental effect of the lack of oxygen, since a reduction in its abundancy results in a lower reaction rate, as could be expected. After fitting these profiles with a monoexponential function in order to obtain the τ values, the plot in Figure 10b was realized, following Equation (6), and a linear regression of the points was performed. The resulting reaction order for oxygen (β) is very close to 1, in agreement with the results of Neeft et al. [57] and Darcy et al. [58] regarding the non-catalytic oxidation of Printex-U soot. Nevertheless, despite this direct dependence of the reaction rate on the oxygen concentration, the Ce50Pr50 catalyst showed promising performances towards soot combustion even in oxygen shortage conditions, thanks to its high intrinsic activity.
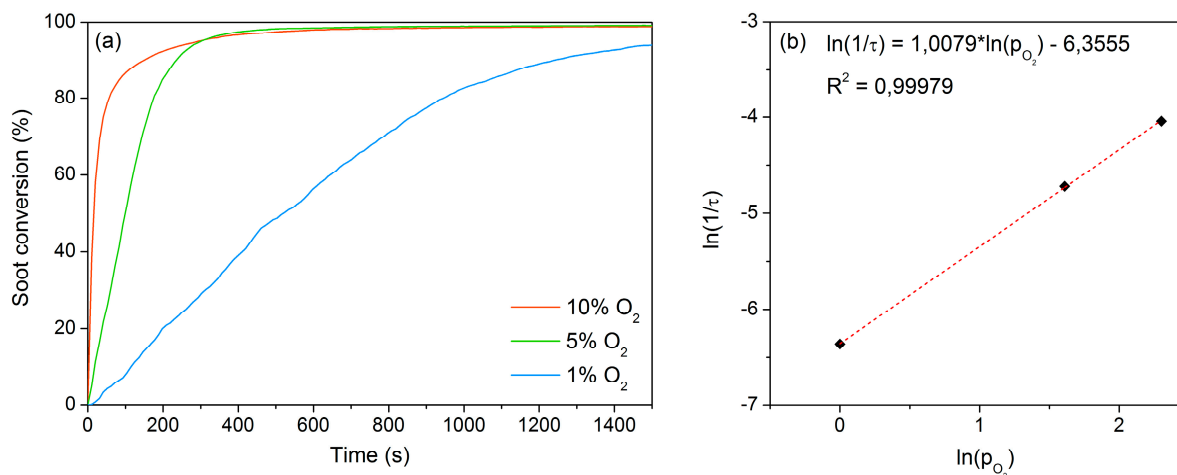
Figure 10. Soot conversion profiles as a function of time during the isothermal soot oxidation tests performed over the Ce50Pr50 catalyst in different O_2 conditions (**a**). Linear regression of the experimental data (**b**), as described in Equation (6).

3. Materials and Methods

3.1. Material Synthesis

The Ce50Pr50 catalyst was prepared via hydrothermal synthesis. Equimolar amounts of $Ce(NO_3)_3 \cdot 6H_2O$ and $Pr(NO_3)3 \cdot 6H_2O$ (10 mmol overall, Sigma-Aldrich, Darmstadt, Germany) were dissolved in 10 mL of deionized water. A second solution was prepared by mixing 48 g of NaOH pellets (Sigma-Aldrich) and 70 mL of deionized water. The solution of lanthanides was then slowly added dropwise into the NaOH solution, under continuous stirring, and a light brown slurry formed. Afterwards, the slurry was stirred at room temperature for 1 h and eventually transferred into the Teflon liner of a stainless-steel autoclave, which was then closed and heated at 180 °C for 24 h inside a furnace. The content of the autoclave was centrifuged and the precipitate was carefully washed by consecutive cycles of suspension and centrifugation in deionized water, ethanol and deionized water again. The washed precipitate was then dried at 60 °C overnight. Finally, the dried powder was gently ground in a mortar and calcined in air at 650 °C for 4 h. A pure CeO_2 sample was prepared for comparison using the same procedure, starting from 10 mmol of $Ce(NO_3)_3 \cdot 6H_2O$.

3.2. Catalyst Characterization

Powder X-ray diffractograms were collected in a Philips X'Pert PW3040 diffractometer using Cu Kα radiation ($\lambda = 1.5418 \times 10^{-10}$ m), with values of 2θ ranging between 20° and 70°, step size of 0.013° and an acquisition time of 0.2 s/step. The diffraction peaks were assigned referring to the Powder Diffraction Files by International Centre of Diffraction Data (ICDD). The crystallite size was estimated using Scherrer's equation; the instrumental peak broadening was corrected using lanthanum hexaboride (LaB_6) as a calibration standard.

Nitrogen physisorption was carried out in a Micromeritics Tristar II 3020, in order to determine the surface area and pore volume of the prepared catalyst. Before the analysis, an outgassing pretreatment was performed by heating the sample at 200 °C for 2 h under nitrogen flow. The specific surface area was calculated with the Brunauer–Emmett–Teller (BET) method.

The morphology of the catalyst was investigated via field emission scanning electron microscopy (FESEM), using a Zeiss Merlin equipped with a Gemini-II column. An Oxford x-act X-ray detector allowed to estimate the sample composition via energy-dispersive X-ray spectroscopy (EDX).

X-ray photoelectron spectroscopy (XPS) was performed in a PHI Versa Probe instrument, using a 187.85 eV band-pass energy, a 45° take-off angle and an X-ray spot size of 100.0 µm.

The catalyst reducibility was investigated via different types of temperature programmed reduction (TPR) analyses. H_2-TPR was performed in a Thermo Scientific 1100 TPDRO equipped with a TCD detector. Some powder (50 mg) was pre-treated by heating it up to 550 °C with a 10 °C/min ramp in He flow. During the analysis, the sample was heated from room temperature up to 800 °C with a 10 °C/min ramp, under a 20 mL/min flow of 5% H_2 in He.

The CO-TPR analysis was carried out in a quartz U-tube reactor (4 mm internal diameter) containing a bed of 150 mg of silica and 45 mg of catalyst powder, placed inside a PID-controlled furnace. Before the analysis, the catalytic bed was pre-treated at 150 °C, flowing 100 mL/min of air for 1 h followed by flushing with N_2 for 30 min. The reactor was then heated from room temperature to 700 °C with a rate of 10 °C/min under a 100 mL/min flow of 2000 ppm of CO in N_2. The concentrations of CO and CO_2 in the outlet were continuously monitored with an ABB Uras 14 non-dispersive infrared (NDIR) analyser.

The soot-TPR was carried out with the same equipment used for CO-TPR. This time, the bed was made of 150 mg of silica, 45 mg of catalyst powder and 5 mg of Printex-U soot, mixed together in a ball mill at 290 rpm for 15 min. Before the analysis, the catalytic bed was pre-treated at 100 °C, flowing 100 mL/min of pure nitrogen for 1 h. The reactor was then heated from room temperature to 800 °C at a rate of 10 °C/min under a 100 mL/min flow of pure N_2. CO and CO_2 in the outlet were monitored with the NDIR analyser.

3.3. Catalytic Activity Tests

The general setup used for the temperature-programmed oxidation (TPO) tests consisted of a PID-controlled furnace, a quartz U-tube reactor with a fixed catalytic bed and a K-type thermocouple with its tip placed as closed as possible to the catalytic bed. A by-pass line was used to let the feed gas concentration stabilize before starting the tests. The CO and CO_2 concentration in the reactor outlet was monitored with an ABB Uras 14 continuous NDIR gas analyser; furthermore, an Emerson XStream X2GP paramagnetic analyser was employed for measuring the concentration of O_2. In the present work, four different TPOs were performed.

3.3.1. CO Oxidation

In this test, the catalytic bed was prepared with 100 mg of catalyst. The bed was pre-treated at 100 °C for 30 min under a 50 mL/min flow of air. The reactor was then cooled to 50 °C, while a mixture of N_2 containing 1000 ppm of CO and 1% or 10% of O_2 was sent to the by-pass line with a flow rate of 50 mL/min. After the concentrations of CO, CO_2 and O_2 had stabilized, the flow was sent to the reactor. Upon reaching the steady state, the gas composition at the outlet was recorded and the oven temperature was increased. The procedure was then repeated in order to sample a sequence of steady states at different temperatures, until the total CO conversion was reached. A blank test was performed in the same way, except preparing the reactor bed with 100 mg of SiO_2.

3.3.2. VOCs Oxidation

Two different tests were carried out to investigate the catalytic activity towards ethylene and propylene complete oxidation. The catalytic bed was prepared with 100 mg of catalyst, and it was pre-treated at 100 °C for 30 min under a 50 mL/min flow of air. The reactor was then cooled to 50 °C, while a mixture of N_2 containing 500 ppm of the VOC (ethylene or propylene) and 1% or 10% of O_2 was sent to the bypass line with a flow rate of 50 mL/min. After the concentrations of CO, CO_2 and O_2 had stabilized, the flow was sent to the reactor. Upon reaching the steady state, the gas composition at the outlet was recorded and the oven temperature was increased. The procedure was then repeated in order to sample a sequence of steady states at different temperatures, until the total VOC conversion was reached. Blank tests were performed in the same way, except the reactor bed was prepared with 100 mg of SiO_2.

3.3.3. Soot Oxidation

The soot oxidation tests were performed on catalytic beds containing 45 mg of catalyst, 150 mg of silica (Sigma-Aldrich) and 5 mg of Printex-U soot (Degussa). Two different contact conditions were investigated: *loose contact* (LC) conditions were obtained by gently mixing the solid mixture with a spatula for three minutes before inserting it in the reactor, while *tight contact* (TC) conditions were obtained by mixing the powders in a ball mill at 290 rpm for 15 minutes. The catalytic bed was pre-treated at 100 °C under a 100 mL/min flow of air for 30 min. Afterwards, a mixture of 1% of O_2 in N_2 was sent with a flow rate of 100 mL/min. The furnace temperature was then raised continuously with a 5 °C/min ramp up to 750 °C.

Isothermal oxidation tests were also performed, preparing a tight contact bed as described above. After the pretreatment, the reactor was flushed with pure nitrogen for some minutes and then sealed. The oven temperature was then raised to 450 °C with a rate of 10 °C/min while a flow of N_2 containing 1%, 5% or 10% O_2 was sent to the bypass line with a flow rate of 100 mL/min. When the goal temperature was reached, the flow was redirected to the reactor and the analysis was carried out until the outlet concentrations of CO and CO_2 were again equal to their baseline values.

4. Conclusions

In this work, a nanostructured equimolar ceria-praseodymia catalyst has been investigated in order to study its behaviour and catalytic activity in low-oxygen conditions. Although Pr ions were well incorporated into the ceria lattice, forming a single phase, the doping caused important structural and morphological changes. Indeed, praseodymium addition affected the crystal growth during the synthesis, resulting in the formation of two different kinds of nanoparticles. Furthermore, Pr weakened the cerium–oxygen bond, allowing to obtain a highly reducible material. Thanks to these properties, the catalyst exhibited a promising activity towards different oxidation reactions, especially in the case of soot combustion. Moreover, its performances only slightly worsened when the oxygen concentration in the inlet gaseous mixture was abated from 10% to 1%. The CO_2 selectivity was very high both in VOCs and soot oxidation, and it was fully preserved in oxygen shortage. These results point out the beneficial effects of coupling the Pr^{4+}-Pr^{3+} redox cycle to that of cerium: indeed, the thus-obtained material is capable of fruitfully delivering active oxygen species to particulate matter and gaseous pollutants. Therefore, equimolar ceria-praseodymia could be suitably employed in catalyzed GPFs, in which a high catalytic activity is required to comply with the emission abatement targets in low oxygen availability.

References

1. Hooftman, N.; Messagie, M.; Van Mierlo, J.; Coosemans, T. A review of the European passenger car regulations – Real driving emissions vs local air quality. *Renew. Sustain. Energy Rev.* **2018**, *86*, 1–21. [CrossRef]
2. Sapio, F.; Millo, F.; Fino, D.; Monteverde, A.; Sartoretti, E.; Bianco, A.; Postrioti, L.; Tarabocchia, A.; Buitoni, G.; Brizi, G. Experimental and Numerical Analysis of Latest Generation Diesel Aftertreatment Systems. *SAE Tech. Pap. Ser.* **2019**, *1*, 18.
3. Johnson, T.; Joshi, A. Review of Vehicle Engine Efficiency and Emissions. *SAE Int. J. Engines* **2018**, *11*, 1307–1330. [CrossRef]
4. Johnson, T. Vehicular Emissions in Review. *SAE Int. J. Engines* **2013**, *6*, 699–715. [CrossRef]
5. Ramos, M.J.M.G.; Wallace, J.S. Fuel Effects on Particulate Matter Emissions Variability from a Gasoline Direct Injection Engine. *SAE Tech. Pap. Ser.* **2018**, 1–17.

6.　Raza, M.; Chen, L.; Leach, F.; Ding, S. A Review of particulate number (PN) emissions from gasoline direct injection (gdi) engines and their control techniques. *Energies* **2018**, *11*, 1417. [CrossRef]

7.　Giechaskiel, B.; Joshi, A.; Ntziachristos, L.; Dilara, P. European Regulatory Framework and Particulate Matter Emissions of Gasoline Light-Duty Vehicles: A Review. *Catalysts* **2019**, *9*, 586. [CrossRef]

8.　Chincholkar, S.P.; Suryawanshi, J.G. Gasoline Direct Injection: An Efficient Technology. *Energy Procedia* **2016**, *90*, 666–672. [CrossRef]

9.　Gao, Y.; Duan, A.; Liu, S.; Wu, X.; Liu, W.; Li, M.; Chen, S.; Wang, X.; Weng, D. Study of Ag/CexNd1-xO2 nanocubes as soot oxidation catalysts for gasoline particulate filters: Balancing catalyst activity and stability by Nd doping. *Appl. Catal. B Environ.* **2017**, *203*, 116–126. [CrossRef]

10.　Bueno-López, A. Diesel soot combustion ceria catalysts. *Appl. Catal. B Environ.* **2014**, *146*, 1–11. [CrossRef]

11.　Trovarelli, A.; Llorca, J. Ceria Catalysts at Nanoscale: How Do Crystal Shapes Shape Catalysis? *ACS Catal.* **2017**, *7*, 4716–4735. [CrossRef]

12.　Piumetti, M.; Bensaid, S.; Andana, T.; Dosa, M.; Novara, C.; Giorgis, F.; Russo, N.; Fino, D. Nanostructured Ceria-Based Materials: Effect of the Hydrothermal Synthesis Conditions on the Structural Properties and Catalytic Activity. *Catalysts* **2017**, *7*, 174. [CrossRef]

13.　Piumetti, M.; Bensaid, S.; Russo, N.; Fino, D. Investigations into nanostructured ceria-zirconia catalysts for soot combustion. *Appl. Catal. B Environ.* **2016**, *180*, 271–282. [CrossRef]

14.　Miceli, P.; Bensaid, S.; Russo, N.; Fino, D. CeO2-based catalysts with engineered morphologies for soot oxidation to enhance soot-catalyst contact. *Nanoscale Res. Lett.* **2014**, *9*, 1–10. [CrossRef] [PubMed]

15.　Fino, D.; Bensaid, S.; Piumetti, M.; Russo, N. A review on the catalytic combustion of soot in Diesel particulate filters for automotive applications: From powder catalysts to structured reactors. *Appl. Catal. A Gen.* **2016**, *509*, 75–96. [CrossRef]

16.　Sartoretti, E.; Novara, C.; Giorgis, F.; Piumetti, M.; Bensaid, S.; Russo, N.; Fino, D. In situ Raman analyses of the soot oxidation reaction over nanostructured ceria-based catalysts. *Sci. Rep.* **2019**, *9*, 3875. [CrossRef]

17.　Wang, H.; Luo, S.; Zhang, M.; Liu, W.; Wu, X.; Liu, S. Roles of oxygen vacancy and Ox− in oxidation reactions over CeO2 and Ag/CeO2 nanorod model catalysts. *J. Catal.* **2018**, *368*, 365–378. [CrossRef]

18.　Polychronopoulou, K.; Zedan, A.F.; AlKetbi, M.; Stephen, S.; Ather, M.; Katsiotis, M.S.; Arvanitidis, J.; Christofilos, D.; Isakovic, A.F.; AlHassan, S. Tailoring the efficiency of an active catalyst for CO abatement through oxidation reaction: The case study of samarium-doped ceria. *J. Environ. Chem. Eng.* **2018**, *6*, 266–280. [CrossRef]

19.　Zhu, H.; Chen, Y.; Wang, Z.; Liu, W.; Wang, L. Catalytic oxidation of CO over mesoporous copper-doped ceria catalysts via a facile CTAB-assisted synthesis. *RCS Adv.* **2018**, 14888–14897. [CrossRef]

20.　Sahoo, T.R.; Armandi, M.; Arletti, R.; Piumetti, M.; Bensaid, S.; Manzoli, M.; Panda, S.R.; Bonelli, B. Pure and Fe-doped CeO2nanoparticles obtained by microwave assisted combustion synthesis: Physico-chemical properties ruling their catalytic activity towards CO oxidation and soot combustion. *Appl. Catal. B Environ.* **2017**, *211*, 31–45. [CrossRef]

21.　Wu, Z.; Li, M.; Overbury, S.H. On the structure dependence of CO oxidation over CeO2nanocrystals with well-defined surface planes. *J. Catal.* **2012**, *285*, 61–73. [CrossRef]

22.　Andana, T.; Piumetti, M.; Bensaid, S.; Russo, N.; Fino, D.; Pirone, R. Nanostructured ceria-praseodymia catalysts for diesel soot combustion. *Appl. Catal. B Environ.* **2016**, *197*, 125–137. [CrossRef]

23.　Andana, T.; Piumetti, M.; Bensaid, S.; Russo, N.; Fino, D. Heterogeneous mechanism of NOx-assisted soot oxidation in the passive regeneration of a bench-scale diesel particulate filter catalyzed with nanostructured equimolar ceria-praseodymia. *Appl. Catal. A Gen.* **2019**, *583*, 117136. [CrossRef]

24.　Guillén-Hurtado, N.; García-García, A.; Bueno-López, A. Active oxygen by Ce-Pr mixed oxide nanoparticles outperform diesel soot combustion Pt catalysts. *Appl. Catal. B Environ.* **2015**, *174–175*, 60–66. [CrossRef]

25.　Andana, T.; Piumetti, M.; Bensaid, S.; Veyre, L.; Thieuleux, C.; Russo, N.; Fino, D.; Quadrelli, E.A.; Pirone, R. Nanostructured equimolar ceria-praseodymia for NOx-assisted soot oxidation: Insight into Pr dominance over Pt nanoparticles and metal–support interaction. *Appl. Catal. B Environ.* **2018**, *226*, 147–161. [CrossRef]

26.　Aneggi, E.; Wiater, D.; De Leitenburg, C.; Llorca, J.; Trovarelli, A. Shape-dependent activity of ceria in soot combustion. *ACS Catal.* **2014**, *4*, 172–181. [CrossRef]

27.　Mukherjee, D.; Rao, B.G.; Reddy, B.M. CO and soot oxidation activity of doped ceria: Influence of dopants. *Appl. Catal. B Environ.* **2016**, *197*, 105–115. [CrossRef]

28. Shannon, R.D. Revised effective ionic radii and systematic studies of interatomic distances in halides and chalcogenides. *Acta Crystallogr. Sect. A* **1976**, *32*, 751–767. [CrossRef]

29. Konsolakis, M.; Carabineiro, S.A.C.; Marnellos, G.E.; Asad, M.F.; Soares, O.S.G.P.; Pereira, M.F.R.; Órfão, J.J.M.; Figueiredo, J.L. Volatile organic compounds abatement over copper-based catalysts: Effect of support. *Inorganica Chim. Acta* **2017**, *455*, 473–482. [CrossRef]

30. Soler, L.; Casanovas, A.; Escudero, C.; Pérez-Dieste, V.; Aneggi, E.; Trovarelli, A.; Llorca, J. Ambient pressure photoemission spectroscopy reveals the mechanism of carbon soot oxidation in ceria-based catalysts. *ChemCatChem* **2016**, *8*, 2748–2751. [CrossRef]

31. Chen, D.; He, D.; Lu, J.; Zhong, L.; Liu, F.; Liu, J.; Yu, J.; Wan, G.; He, S.; Luo, Y. Investigation of the role of surface lattice oxygen and bulk lattice oxygen migration of cerium-based oxygen carriers: XPS and designed H2-TPR characterization. *Appl. Catal. B Environ.* **2017**, *218*, 249–259. [CrossRef]

32. Bensaid, S.; Piumetti, M.; Novara, C.; Giorgis, F.; Chiodoni, A.; Russo, N.; Fino, D. Catalytic Oxidation of CO and Soot over Ce-Zr-Pr Mixed Oxides Synthesized in a Multi-Inlet Vortex Reactor: Effect of Structural Defects on the Catalytic Activity. *Nanoscale Res. Lett.* **2016**, *11*, 1–14. [CrossRef] [PubMed]

33. Pappacena, A.; Rancan, M.; Armelao, L.; Llorca, J.; Ge, W.; Ye, B.; Lucotti, A.; Trovarelli, A.; Boaro, M. New Insights into the Dynamics That Control the Activity of Ceria-Zirconia Solid Solutions in Thermochemical Water Splitting Cycles. *J. Phys. Chem. C* **2017**, *121*, 17746–17755. [CrossRef]

34. Hernández, S.; Gionco, C.; Husak, T.; Castellino, M.; Muñoz-Tabares, J.A.; Tolod, K.R.; Giamello, E.; Paganini, M.C.; Russo, N. Insights Into the Sunlight-Driven Water Oxidation by Ce and Er-Doped ZrO2. *Front. Chem.* **2018**, *6*, 368. [CrossRef] [PubMed]

35. Poggio-Fraccari, E.; Baronetti, G.; Mariño, F. Pr3+ surface fraction in CePr mixed oxides determined by XPS analysis. *J. Electron Spectros. Relat. Phenomena* **2018**, *222*, 1–4. [CrossRef]

36. Piumetti, M.; Andana, T.; Bensaid, S.; Fino, D.; Russo, N.; Pirone, R. Ceria-based nanomaterials as catalysts for CO oxidation and soot combustion: Effect of Zr-Pr doping and structural properties on the catalytic activity. *AIChE J.* **2017**, *63*, 216–225. [CrossRef]

37. Jin, J.; Li, C.; Tsang, C.W.; Xu, B.; Liang, C. Catalytic combustion of methane over Pd/Ce-Zr oxides washcoated monolithic catalysts under oxygen lean conditions. *RSC Adv.* **2015**, *5*, 102147–102156. [CrossRef]

38. Tong, X.; Luo, T.; Meng, X.; Wu, H.; Li, J.; Liu, X.; Ji, X.; Wang, J.; Chen, C.; Zhan, Z. Shape-Dependent Activity of Ceria for Hydrogen Electro-Oxidation in Reduced-Temperature Solid Oxide Fuel Cells. *Small* **2015**, *11*, 5581–5588. [CrossRef]

39. Reddy, B.M.; Thrimurthulu, G.; Katta, L. Design of efficient CexM1-xO2-δ (M = Zr, Hf, Tb and Pr) nanosized model solid solutions for CO oxidation. *Catal. Lett.* **2011**, *141*, 572–581. [CrossRef]

40. Dosa, M.; Piumetti, M.; Bensaid, S.; Russo, N.; Fino, D. Novel Mn–Cu-Containing CeO 2 Nanopolyhedra for the Oxidation of CO and Diesel Soot (Part II): Effect of Oxygen Concentration on the Catalytic Activity. *Catal. Lett.* **2019**, *149*, 107–118. [CrossRef]

41. Schmitz, T.; Hassel, D.; Weber, F.J. Determination of VOC-components in the exhaust of gasoline and diesel passenger cars. *Atmos. Environ.* **2000**, *34*, 4639–4647. [CrossRef]

42. Kampa, M.; Castanas, E. Human health effect of air polution-Enviro Polution-08.pdf. *Environ. Pollut.* **2008**, *151*, 362–367. [CrossRef] [PubMed]

43. Zhang, Z.; Jiang, Z.; Shangguan, W. Low-temperature catalysis for VOCs removal in technology and application: A state-of-the-art review. *Catal. Today* **2016**, *264*, 270–278. [CrossRef]

44. Pappas, G.P.; Herbert, R.J.; Henderson, W.; Koenig, J.; Stover, B.; Barnhart, S. The respiratory effects of volatile organic compounds. *Int. J. Occup. Environ. Health* **2000**, *6*, 1–8. [CrossRef]

45. Shao, M.; Zhang, Y.; Zeng, L.; Tang, X.; Zhang, J.; Zhong, L.; Wang, B. Ground-level ozone in the Pearl River Delta and the roles of VOC and NOx in its production. *J. Environ. Manag.* **2009**, *90*, 512–518. [CrossRef]

46. Dziembaj, R.; Molenda, M.; Chmielarz, L.; Zaitz, M.M.; Piwowarska, Z.; Rafalska-Łasocha, A. Optimization of Cu doped ceria nanoparticles as catalysts for low-temperature methanol and ethylene total oxidation. *Catal. Today* **2011**, *169*, 112–117. [CrossRef]

47. Liotta, L.F.; Ousmane, M.; Di Carlo, G.; Pantaleo, G.; Deganello, G.; Marcì, G.; Retailleau, L.; Giroir-Fendler, A. Total oxidation of propene at low temperature over Co3O4-CeO2 mixed oxides: Role of surface oxygen vacancies and bulk oxygen mobility in the catalytic activity. *Appl. Catal. A Gen.* **2008**, *347*, 81–88. [CrossRef]

48. Piumetti, M.; Bensaid, S.; Andana, T.; Russo, N.; Pirone, R.; Fino, D. Cerium-copper oxides prepared by solution combustion synthesis for total oxidation reactions: From powder catalysts to structured reactors. *Appl. Catal. B Environ.* **2017**, *205*, 455–468. [CrossRef]

49. Dole, H.A.E.; Baranova, E.A. Ethylene Oxidation in an Oxygen-Deficient Environment: Why Ceria is an Active Support? *ChemCatChem* **2016**, *8*, 1977–1986. [CrossRef]

50. Lang, W.; Harold, M.P. Rate Inhibition and Enhancement on Ceria-Promoted Pd Monolith Catalysts: Oxidation of Acetylene, Ethylene, and Propylene and Their Mixtures. *Ind. Eng. Chem. Res.* **2019**, *58*, 6350–6363. [CrossRef]

51. Piumetti, M.; van der Linden, B.; Makkee, M.; Miceli, P.; Fino, D.; Russo, N.; Bensaid, S. Contact dynamics for a solid-solid reaction mediated by gas-phase oxygen: Study on the soot oxidation over ceria-based catalysts. *Appl. Catal. B Environ.* **2016**, *199*, 96–107. [CrossRef]

52. Di Sarli, V.; Landi, G.; Lisi, L.; Saliva, A.; Di Benedetto, A. Catalytic diesel particulate filters with highly dispersed ceria: Effect of the soot-catalyst contact on the regeneration performance. *Appl. Catal. B Environ.* **2016**, *197*, 116–124. [CrossRef]

53. Di Sarli, V.; Di Benedetto, A. Combined effects of soot load and catalyst activity on the regeneration dynamics of catalytic diesel particulate filters. *AIChE J.* **2018**, *64*, 1714–1722. [CrossRef]

54. Di Sarli, V.; Landi, G.; Lisi, L.; Di Benedetto, A. Ceria-coated diesel particulate filters for continuous regeneration. *AIChE J.* **2017**, *63*, 3442–3449. [CrossRef]

55. Boger, T.; Rose, D.; Nicolin, P.; Gunasekaran, N.; Glasson, T. Oxidation of Soot (Printex®U) in Particulate Filters Operated on Gasoline Engines. *Emiss. Control Sci. Technol.* **2015**, *1*, 49–63. [CrossRef]

56. Kastrinaki, G.; Lorentzou, S.; Konstandopoulos, A.G. Soot Oxidation Kinetics of Different Ceria Nanoparticle Catalysts. *Emiss. Control Sci. Technol.* **2015**, *1*, 247–253. [CrossRef]

57. Neeft, J.P.A.; Nijhuis, T.X.; Smakman, E.; Makkee, M.; Moulijn, J.A. Kinetics of the oxidation of diesel soot. *Fuel* **1997**, *76*, 1129–1136. [CrossRef]

58. Darcy, P.; Da Costa, P.; Mellottée, H.; Trichard, J.M.; Djéga-Mariadassou, G. Kinetics of catalyzed and non-catalyzed oxidation of soot from a diesel engine. *Catal. Today* **2007**, *119*, 252–256. [CrossRef]